



Numerical simulations of zigzag maneuver of free running ship in waves by RANS-Overset grid method

Jianhua Wang, Lu Zou, Decheng Wan

Show more

Outline | Share | Cite

<https://doi.org/10.1016/j.oceaneng.2018.05.021>

Get rights and content

Highlights

- A dynamic overset grid is applied to directly simulate a twin screw fully appended ship by CFD method.
- Zigzag maneuver in waves is calculated incorporating for an appended ship having rotating propellers and turning rudders.
- Wave length and wave height influences on free running zigzag maneuver are extensively studied using RANS-overset method.
- Extensive comparisons with experiments are undertaken and satisfactory agreements are observed for parameters of interest.
- Detailed flow visualizations are presented to give a better understanding of hydrodynamic influences on ship performance.

Abstract

The twin-screw fully appended ONR Tumblehome ship model is numerically studied for the standard 10/10 zigzag maneuver. Simulations are carried out using naoe-FOAM-SJTU, a CFD solver developed on open source platform, OpenFOAM. Overset grid technique and 6DoF module with a hierarchy of bodies are applied to solve the motions of the free-running ship with twin rotating propellers and turning rudders. The self-propulsion point is using the constant value obtained by the previous CFD simulation of the twin-screw self-propelled ship in calm water. Simulations of the standard zigzag maneuver in both calm water and different incident waves are considered. The present CFD results agree well with the available experimental measurement for both ship motions and the main parameters of zigzag maneuver. This indicates that the direct simulations for ship zigzag maneuver in waves utilizing present methods are feasible and reliable. In addition, it is found that unsteady effects of the hydrodynamic loads on the free-running ship during zigzag maneuver in waves is noticeable. Furthermore, flow visualizations in different incident waves are presented so as to give a better understanding of the wave influences on free-running ship maneuver.

Previous

Next

Keywords

Zigzag maneuver in waves; Twin-screw ship; RANS-overset grid method; naoe-FOAM-SJTU solver

1. Introduction

Ship maneuver is closely related to the navigational safety. When considering ship maneuver in waves, it will further strongly interact with the seakeeping performance, thus making the evaluation of ship maneuverability more complicated and difficult. Recently, the research of maneuvering in waves is becoming increasingly popular, consequently, a specialist committee which is responsible for maneuvering in waves is established by the 28th International Towing Tank Conference (ITTC, 2017a). Generally, ship maneuver experiences large low-frequency motions in calm water while in waves it encounters high-frequency wave induced motions. Free-running ship maneuver in most cases is conducted by executing rudders along with rotating propellers, and it becomes more complicated when evaluating the performance of fully appended ship in waves. As one of the most difficult problems in the research of ship hydrodynamics, the accurate prediction of ship maneuvering performance during free-running motion through either experimental or numerical method is still challenging.

Traditional experimental test in a conventional towing tank or wave basin still plays an important role in predicting the ship maneuvering and seakeeping behaviors. However, the increasing demand of applying self-propelled ships when conducting free-running ship model tests also proposes a higher requirement of the measurement facility. For instance, extensive experiments have been done at the Iowa Institute of Hydraulic Research (IIHR) wave basin for free-running ship maneuver in both calm water and waves (Araki et al., 2012; Sanada et al., 2013), which provided plenty of reliable experimental data. Sprenger et al. (2017) has done turning circle tests in Marintek wave basin within the SHOPERA project. However, the high cost of the experimental measurements and the complexity in local flow measurement still hold back its application, and this is the reason why the experiment measurements are only required at the final design stage.

Besides the experiment measurements, several numerical approaches have been proposed to study the ship maneuvering and seakeeping problems. System-based simulation (SBS) (Sakamoto et al., 2012; Simonsen et al., 2012) is a traditional method for modeling ship maneuvering motion. However, SBS require a large number of data from experiments or Computational Fluid Dynamics (CFD) simulated results to predict maneuvering performance, therefore the prediction is strongly dependent on the available database. Potential theory (Fonseca and Guedes Soares, 1998; Pérez Arribas, 2007) can be very fast to give predicted results for ship motion in waves. Unfortunately, since both SBS method and potential theory rely on the simpler mathematical modeling by not directly simulating the moving appendages, it is nearly impossible to give reliable and accurate results of the unsteady local flows around the fully appended hull with complex geometries such as rotating propellers and turning rudders.

Previously, people use mathematical models to predict the maneuvering motion, at the same time, they calculate the wave induced motions according to the potential theory. Zhang and Zou (2015) applied the 4 degrees of freedom (4DoF) Maneuvering Modeling Group (MMG) model to solve ship maneuvering motion and they determined the high frequency wave induced motions by solving a linearized boundary value problem (BVP) in time domain. Nonetheless, there is a large discrepancy between their predicted results and experiment data, which shows that the potential theory actually cannot accurately describe the maneuvering characters in waves. Seo and Kim (2011) applied a similar approach to model the maneuvering motion and wave induced ship response. Their results show reasonable agreement but less accuracy. Therefore, CFD methods are preferable in the predictions of ship maneuvering and seakeeping performances. Direct CFD simulations are able to provide accurate prediction of hydrodynamic locals and specific local flow details since they can well resolve the complex flows around the hull and its appendages. But due to the high computational cost and complex numerical models, only few free-running simulations have been performed by CFD approach, and the number is even less for the free-running in waves.

So far, the most reliable and robust approach to simulate free-running ship maneuver is the dynamic overset grid method coupled with full 6DoF motion solver with a hierarchy of bodies. This approach was firstly introduced to ship and ocean engineering for CFD simulations of self-propelled ships (Carrica et al., 2010; Castro et al., 2011) without rudder. With the dynamic overset grid technique, simulations of ship maneuvers with active rudders became feasible. Carrica et al. (2012) simulated the turn and zigzag maneuver by using a Reynolds-Average Navier-Stokes (RANS) approach

where the deflection of rudders were achieved by the dynamic overset grid technique with a hierarchy of hull and rudders, while the rotating propellers were simplified by body forces. Furthermore, Carrica et al. (2012) performed maneuver simulations in waves by using the simplified model and found that the main discrepancy between the CFD and experiments can possibly be tracked to the simplistic propeller model. Mofidi and Carrica (2014) presented the direct simulation of free-running zigzag maneuver for a single screw KRISO Container Ship (KCS), where standard 10/10 zigzag maneuver and modified 15/1 zigzag maneuver with actual rotating propeller and turning rudder were computed in calm water. The results were promising when compared with the experiment, although the authors emphasized that the computational cost in direct calculating free-running ships was still very high. Carrica et al. (2016) further extended the direct simulation of zigzag maneuver of KCS ship model in shallow water with rather low approaching speed. The CFD results agreed well with the experiment data for most hydrodynamic quantities. Broglia et al. (2015) and Dubbioso et al. (2016) used a similar overset grid approach to simulate the turning circle maneuver in calm water by using a finite volume method CFD solver. The ship model was a fully appended twin-screw vessel with a single rudder. The twin rotating propellers were simulated by an actuator disk model, which was modified to account for oblique flow effects. Further analysis for the distribution of forces and moments on the hull and appendages was done to obtain the hydrodynamic behavior in turning tests. Recently, Dubbioso et al. (2017) and Muscari et al. (2017) conducted CFD investigations of propeller bearing loads in steady and transient maneuvers using overset grid approach. Shen et al., 2015, Shen et al., 2014 implemented the dynamic overset grid module to the open source CFD software OpenFOAM and presented some applications to the turn and zigzag maneuvering simulations for benchmark ship models, such as KCS, KRISO Very Large Crude Carrier (KVLCC2), US Navy Combatant (DTMB5415). Unlike previous studies, the unstructured overset grid technique was introduced, which showed impressive flexibility and efficiency of the mesh generation for complex geometries. Their results agreed well with the experimental data, indicating that the fully discretized model with overset grid method was feasible even for the relatively coarse unstructured grids. Wang et al. (2016) used the same approach to simulate the self-propulsion and turning circle maneuver of the fully appended twin-screw Office of Naval Research (ONR) Tumblehome model in calm water. The predicted ship motions for the maneuvering conditions agreed well with the available experimental data.

Most of previous studies on ship maneuver with free-running ship models only focus on the calm water conditions and most of them only used the simplified propeller model, which cannot accurately capture the unsteady local flows. In particular, with such a model the effects of the rotating propeller are missing. However, a precise simulation of ship maneuvering in waves inevitably has to consider large-amplitude ship motions with more violent free surface deformation and more notable hull-propeller-rudder interactions, which is more difficult than the simulation in calm water. Wang et al. (2017) extended the free-running simulations from calm water to waves for a course-keeping problem and showed the capability of CFD with dynamic overset grid in predicting ship maneuvering in waves. In the present paper, more emphasis is put on the free-running zigzag maneuver under various wave conditions for a fully appended twin-screw ship. The motivation of this study is to find out whether it is reliable for the numerical computations of free-running zigzag maneuver in waves and to study the wave effects on the ship maneuver.

This paper is organized as follows: the computational methods are presented in the second section; the simulation designs, including the geometry model, test conditions and grid distribution are described in the third section; the simulation results and discussions are presented in the fourth section; finally, conclusions from the present study are made.

2. Computational methods

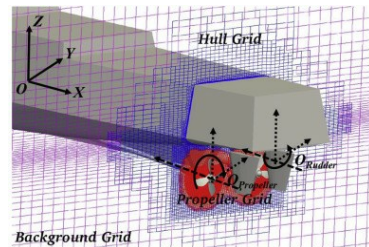
The computations are performed with the ship hydrodynamics CFD solver, naoe-FOAM-SJTU, developed on an open source platform OpenFOAM. It is easy to achieve the free-running ship maneuvering motion (see Section 2.1) since this solver has the dynamic overset grid capability and includes a full 6DoF motion module with a hierarchy of bodies. In general, naoe-FOAM-SJTU solves the Reynolds-averaged Navier-Stokes (RANS) equations for unsteady turbulent flows around complex geometries. For capturing the free surface elevation, a volume of fluid (VOF) approach with bounded compression technique is used (Berberović et al., 2009). The turbulence features are modeled by a blended $k - \omega k - \epsilon$ shear stress transport (SST) turbulence model (Menter et al., 2003). Wall functions are used to model the velocity gradient effects near the wall. The solver has been extensively validated on large amount of ship hydrodynamic cases, e.g. ship resistance (Zha et al., 2015), seakeeping (Shen and Wan, 2013, 2016; Wang and Wan, 2016) and maneuvering (Shen et al., 2015; Wang et al., 2016, 2017).

The computational domain is discretized by multi unstructured overlapping grids, and the finite volume method (FVM) is used to transform the equations from physical space into computational space. Besides, the pressure-implicit split-operator (PISO) algorithm (Issa, 1986) is applied for pressure-velocity coupling in solving governing equations. In addition, several built-in discretization schemes in OpenFOAM are used to solve the partial differential equations (PDE): the implicit Euler scheme is used for temporal discretization; second order total variation diminishing (TVD) scheme is used to discretize the convection term in momentum equation; a central differencing scheme is applied for diffusion terms.

2.1. Dynamic overset grid and maneuvering control

The dynamic overset grid technology and full 6DoF motion method with a hierarchy of bodies are crucial to simulate the free-running ship maneuver including complex geometries with independent motions e.g. rotating propellers and turning rudders. Generally, overset grid includes two or more blocks of overlapping structured or unstructured grids, and the value of a flow variable in the fringe cell is obtained by interpolation from the donor cells. In the present work, Suggar++ library (Noack et al., 2009) is utilized to obtain the overset connectivity at run time. More details about the overset grid implementation in OpenFOAM can be found in Shen et al. (2015) and Wang et al. (2017).

With dynamic overset grid, 6DoF motion solver is incorporated with a hierarchy of bodies, which allows the ship and its appendages (propellers, rudders, etc.) to move simultaneously. Fig. 1 gives a general description of overset grids for ship and its appendages with the coordinate systems for motion controls. During the calculation, the ship moves according to the 6DoF equations, the propellers and rudders follow the ship with the same forward speed but can translate or rotate in their own systems based on special control mechanism. When handling with the motion of overlapping grids in computations, the propeller or rudder grid blocks taken to be the children level first rotate or turn according their control laws. Then they move together with the ship grid block (parent level) according to the ship motion obtained by 6DoF equations. Finally, the background grid, which connects the ship to farfield boundary, follows the ship with surge, sway and yaw motion so that the free surface stays horizontal.



[Download : Download high-res image \(701KB\)](#)

[Download : Download full-size image](#)

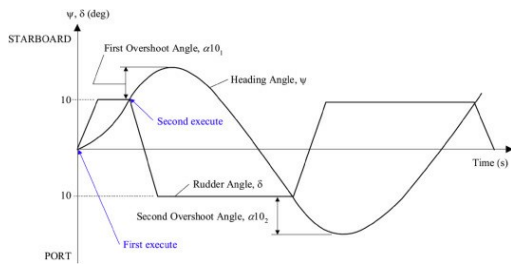
Fig. 1. Overset grids and coordinate systems for motions.

Two coordinate systems are used to solve the 6DoF equations based on Euler angles. The flow equations are solved in the inertial system (earth-fixed system) and the calculated forces and moments are then transformed to the non-inertial system (ship-fixed system), where the rigid-body equations are solved. In the present work, the 6DoF motion equations are solved using a semi-implicit approach, where the solution is given by iterations to fulfil convergence and more detailed information of 6DoF motion solver can be found in Shen et al. (2015).

Regarding the maneuvering control, this study adopts the open loop of feedback controllers under specified requirement of desired ship motion, such as the rotational speed of propeller, heading control and roll control etc. For zigzag maneuver, the ship is moving forward with nominal constant speed and the rudder is executed to a specified maximum rudder angle at the maximum rudder rate. Then the ship responses with a turning motion due to the rudder deflection, which can be used to access the ship maneuverability. As for the zigzag maneuver simulated in the present work, the rudder deflection for the standard 10/10 zigzag maneuver follows:

$$\delta(t) = \begin{cases} \min(\kappa t, 10), & t_1 \leq t \leq t_2 \\ \max(-\kappa t - 10), & t_2 \leq t \leq t_3 \\ \min(\kappa t, 10), & t_3 \leq t \leq t_4 \end{cases} \quad (1)$$

where $\delta(t)$ is the rudder angle, which is positive when the rudder turns to the starboard side; κ is the maximum rudder rate which is provided by the model test, t_1 is the time for rudder execution. In addition, Fig. 2 demonstrates the main parameters in a standard 10/10 zigzag maneuver, such as the first and second overshoot angle (OSA) of the ship (the excess angle between the maximum/minimum ship's heading and the check heading angle), the period (time to complete one zigzag cycle) etc.



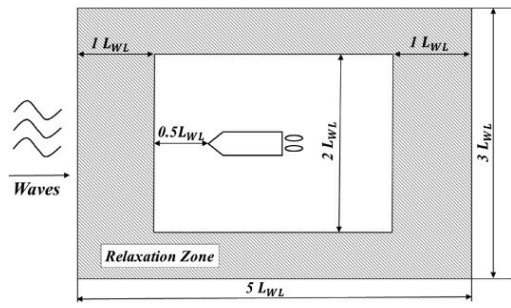
[Download : Download high-res image \(165KB\)](#)

[Download : Download full-size image](#)

Fig. 2. Main parameters in 10/10 zigzag maneuver (ABS, 2006).

2.2. Wave generation

In the present simulations, the computational domain, namely, the background grid is moving forward with the ship horizontal motion. Therefore, the `velocity-inlet` boundary condition for wave generation may not be appropriate since the boundary may deviate from its original position. In order to generate desired wave environment with the moving computational domain, the open source toolbox `waves2foam` (Jacobsen et al., 2012) is used for all the computations. The methodology adopts the relaxation zones to avoid reflections of waves from outlet boundaries and further to avoid `waves_reflected` internally in the computational domain to interfere with the wave maker boundaries. The flow parameters, such as velocity v and volume of fraction α , can be blended by a relaxation factor γ_α . The details of the relaxation technique can be found in Jacobsen et al. (2012). The schematic of the computational domain and wave generation zone is shown in Fig. 3. A frozen type relaxation zone is used in the present simulations so that the wave generation zone can move with the computational domain, This guarantees that the waves can propagate to the area around ship model no matter how the computational domain rotates or translates. In the present work, the first-order Stokes wave theory with specified wave parameters is adopted.



[Download : Download high-res image \(829KB\)](#)

[Download : Download full-size image](#)

Fig. 3. Schematic of the computational domain and wave generation zone.

3. Simulation design

3.1. Geometry model

ONR Tumblehome model 5613 is a preliminary design of a modern surface combatant fully appended with `skeg` and `bilge keels`. In addition, the model is equipped with twin rudders, shafts and twin `propellers` with propeller shaft brackets. It is one of the benchmark ship models in 2015 Tokyo CFD Workshop in ship hydrodynamics and has extensive experimental data. The geometry of ONR Tumblehome ship model is shown in Fig. 4, and main particulars are listed in Table 1.



[Download : Download high-res image \(36KB\)](#)

[Download : Download full-size image](#)

Fig. 4. Geometry model of ONR Tumblehome.

Table 1. Main particulars of ONR Tumblehome ship model.

Main particulars	Symbols	Model scale (1:49)
Length of waterline	L_{WL} (m)	3.147
Maximum beam of waterline	B_{WL} (m)	0.384
Draft	T (m)	0.112
Displacement	Δ (kg)	72.6
Wetted surface area (fully appended)	S_w (m^2)	1.5
Block coefficient	γ ($L_{WL} B_{WL} T$)	0.535
Longitudinal center of gravity	L_{CG} (m) α_{fP} (F_P)	1.625
Vertical center of gravity	KG (m)	0.156
Moment of inertia	K_{xz}/B	0.444
Propeller diameter	K_{xz}/L_{WL} K_{xz}/L_{CG}	0.246
Propeller shaft angle (downward positive)	δ_P (deg.)	5
Propeller rotation direction (view from stern)		inward
Maximum rudder rate	(deg./s)	35.0

3.2. Grid distribution

The computational domain is divided into six parts according to the motion level of overset grid topology: one for the background grid, one for the grid around the ship hull, two for the grids around the two propellers on starboard side and port side respectively, two parts for the two rudders. For the overset grids arrangement, the background domain extends to $-1.5L_{tw_1} < x < 3.5L_{tw_1}$, $-1.5L_{tw_1} < z < 1.5L_{tw_1}$, $-1.0L_{tw_1} < z < 0.5L_{tw_1}$, and the hull domain is much smaller with a range of $-0.15L_{tw_1} < x < 1.2L_{tw_1}$, $-0.13L_{tw_1} < y < 0.13L_{tw_1}$, $-0.2L_{tw_1} < z < 0.2L_{tw_1}$. The detailed overset grid arrangements are shown in Fig. 5a. Unstructured grids are generated by the pre-processing utilities provided by OpenFOAM. Overset grid topology around solid surfaces is shown in Fig. 5b. Near-wall grid spacing is designed to meet the requirement of turbulence model using wall functions, where the Y^+ is around 60. The total grid number for the free-running simulations is around 7 million, where the background grid varies in different simulation cases. The motion of each part grid which follows the control laws of free-running ship maneuver is discussed in section 2.1.

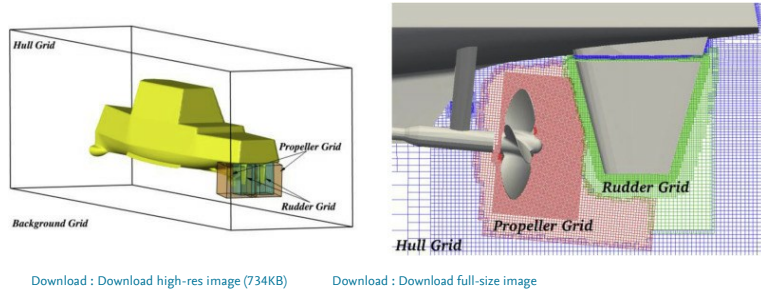


Fig. 5. Overset grid arrangement and distribution.

As for the boundary conditions of the computational domain, the inlet and relaxation zone as shown in Fig. 3 is used to generate desired waves. The conditions of velocity and volume of fraction are imposed by the specified first-order Stokes wave theory; the farfield boundaries are identical with zero velocity and zero gradient of pressure; the surfaces of the moving bodies are non-slip and the outlet is specified by the downstream boundaries.

Once all the grids are generated, a preprocessing step requires setting up and running SUGAR++ with appropriate boundary conditions, with the aim of checking the validity of interpolations among different grid blocks. It should be emphasized that artificial gaps between propellers and shafts, rudders and rudder roots are reserved to obtain enough fringe-donor cells for the overlapping grid interpolation. The positions and geometries of the rudders and propellers remain unchanged and only the shafts and rudder roots are slightly adjusted to keep the gaps. Another procedure before the simulations started is a simple hydrostatic computation, which is used to obtain the longitudinal location of the center of buoyancy, the displacement and the static wetted area of the ship in even keel condition with the discretized computational model. The resulting displacement of the ship model is 0.07% larger than the value used in the experiment. The small deviation is due to the spatial discretization error of the geometry.

3.3. Test conditions

All the simulations conditions are defined based on two non-dimensional numbers: the Reynold number $Re = U_b L_{W.L} / v$ and the Froude number $F_F = U_b / \sqrt{g L_{W.L}}$, where v is the kinematic viscosity, g is the gravitational acceleration. All the computations of the free-running ship maneuver are at the same approaching speed of 1.11 m/s in model scale, corresponding to $F_F = 0.20$.

According to the model tests, the self-propelled ship was set to advance at model point with full 6DoF motion in both calm water and regular waves. In CFD simulations, the self-propulsion test must be performed to obtain the self-propulsion point and then the model point is used for the free-running ship maneuver simulations. This work has already been done in the previous work (Wang et al., 2017) and the CFD results of the rotational speed of twin propeller is 8.819 resolutions per second (RPS), which is reasonable when compared with the experiment data of 8.97 RPS. In the present calculations of zigzag maneuver in waves, the same rotational speed of twin propellers obtained by the previous work is applied and is kept constant during the maneuver simulations. Using a fixed rotational speed in the free-running ship maneuver simulations can reduce the difficulty and uncertainties, and help CFD researcher to validate their numerical approaches, since it is quite challenging for CFD simulations to repeat exactly the same conditions as in the experiment. The details of test cases are shown in Table 2. Zigzag maneuver simulations are firstly performed under calm water conditions due to its simplicity, then five wave conditions are considered with the combination of three wave lengths and three wave steepness.

Table 2. Test conditions for zigzag maneuver simulations.

Cases	Wave length (m)	λ / L_{tw_1}	Wave height		Wave steepness H/A
			A (m)	B (m)	
Calm water	NA	NA	NA	NA	NA
Waves	1.5735	0.5	0.03147	0.06294	0.02
	3.147		0.06294	0.06294	0.04
	3.7764	1.0	0.077528	0.06294	0.02
					0.0167

4. Numerical simulations and discussions

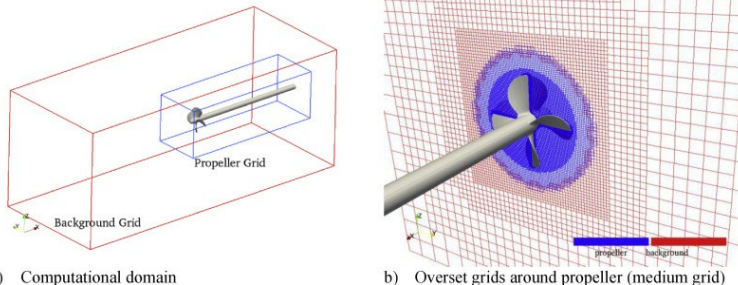
All the calculations are conducted on the HPC cluster center in Computational Marine Hydrodynamics Lab (CMHL), Shanghai Jiao Tong University. Each node consists of 2 CPUs with 20 cores per node and 64 GB accessible memory (Intel Xeon E5-2680v2 @2.8 GHz).

4.1. Grid convergence study

According to the literature involving simulations of free running ship maneuver with dynamic overset grid, the grid refinement will strongly affect the quality of overlapping grids, especially for the complex hull-propeller-rudder system, where the gaps between each component are very small. As a result, a grid convergence study for such complicated problem is rarely done by the researchers. In the present work, open water calculations with simpler overset grid arrangements are employed for the grid convergence study. The open water case is a proper candidate for the grid convergence study with the fact that the computations for rotating propeller are crucial for the simulations for self-propelled ships.

Open water calculation follows the experimental setup available at Tokyo 2015 CFD Workshop, where the rate of resolution of propeller is fixed with value of 8.97 RPS. The computational domain is divided into two parts, i.e. background grid and propeller grid as shown in Fig. 6a. During the calculation, the propeller grid rotates with the rotating propeller while the background grid moves forward with the advancing velocity. Three grids with a refinement ratio of $\sqrt{2}$ in each direction are used for grid convergence study, which follows the recommended procedures and guidelines (ITTC, 2017b). Result changes between medium-fine $\varepsilon_{21} = S_2 - S_1$ and coarse-medium $\varepsilon_{31} = S_3 - S_1$ are used to define the convergence ratio R_G :

$$R_G = \frac{\varepsilon_{21}}{\varepsilon_{31}} \quad (2)$$



a) Computational domain

[Download : Download high-res image \(987KB\)](#)

b) Overset grids around propeller (medium grid)

[Download : Download full-size image](#)

Fig. 6. Computational domain and overset grid distribution for open water calculation.

And R_G is used to determine convergence condition, where s_i, s_j and s_k correspond to solutions with fine, medium, and coarse grid, respectively. Three convergence conditions are possible:

- (i) $0 < R_G < 1$ Monotonic convergence
 - (ii) $R_G < 0$ Oscillatory convergence
 - (iii) $R_G > 1$ Divergence
- (3)

For condition (III), grid convergence study cannot be estimated. Hydrodynamic parameters K_T , K_Q and η are used to estimate the grid convergence. The propulsion coefficients mentioned above are defined as:

$$J = \frac{v_a}{\pi D_p} \quad (4)$$

$$K_T = \frac{T}{\rho v_a^2 D_p} \quad (5)$$

$$K_Q = \frac{Q}{\rho v_a^2 D_p} \quad (6)$$

$$\eta = \frac{JK_T}{2\pi K_Q} \quad (7)$$

where T and Q are the propeller thrust and torque, D_p is the diameter of propeller, n is the RPS and v_a is the advancing speed. Grid distribution around propeller for medium grid is shown in Fig. 6b. For all three grids, the resulting Y^* varies from 40 to 120 with the consideration of wall function are applied near wall. The grid convergence study is carried out at $J = 1.0$ for the open water case with respect to the most approximate condition to the propeller at self-propulsion and zigzag maneuver simulation.

During the computation, the time step was set to a rather small value of $\Delta t = 0.0005$ s in order to resolve the transient flow due to the rotating propeller, which corresponds to approximately 1.5° of propeller rotation per time step, and the resultant **Courant number** is around 0.1. 20 processors are assigned to calculate the open water case, in which 19 processors are for the flow calculation and another processor is used for SUGAR++ calculation. It costs approximately 30, 55 and 122 h to complete the computations for coarse, medium and fine grid cases, respectively. Table 3 summarizes the results of the grid convergence study for open water calculations.

Table 3. Grid convergence study of open water calculations.

Grid	ID	Grid Size	K_T	Error (%)	K_Q	Error (%)	η	Error (%)
EFD			0.2638		0.0734		0.5723	
Fine	s_i	3.892M	0.2635	-0.113	0.0763	3.951	0.5496	-3.966
Medium	s_j	1.233M	0.2632	-0.226	0.0782	6.539	0.5357	-6.395
Coarse	s_k	0.576M	0.2594	1.668	0.0806	9.809	0.5122	-10.501
R_G			0.0789		0.7916		0.5915	
Convergence			Monotonic		Monotonic		Monotonic	

It can be seen from Table 3 that the thrust coefficient K_T shows monotonic convergence with $R_G = 0.0789$ and the predicted value of K_T is highly accurate with errors lower than 1.7%. The torque coefficient K_Q is overestimated by all three grids with errors up to 9.8% and the efficiency η is underestimated with largest error of -10.5%. Both torque coefficient and efficiency show monotonic convergence with $R_G = 0.7916$ and 0.5915, respectively.

Note that the grid size of propellers in free running zigzag maneuver simulation is larger than medium grid but smaller than the fine grid. This indicates that the propeller grid used in the free running ship maneuver simulation will slightly change the numerical results.

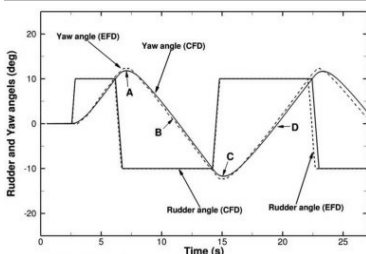
4.2. Zigzag maneuver in calm water

For the simulations of free running ship maneuver in both calm water and waves, 40 processors are adopted, in which 38 processors are for the flow calculation and the other 2 processors are used for SUGAR++ calculation. The time step was set to $\Delta t = 0.0005$ s, which is according to the previous open water calculations. It costs approximately 325 h of clock time with about 39000 time steps to complete the computation in calm water, while 347 h for the cases in waves.

The simulation case of standard 10/10 zigzag maneuver in calm water is used to validate the present CFD method due to its simplicity. Furthermore, the calm water computation can give the guidance of numerical setup for the free-running ship maneuver computations in waves, and most importantly to be a useful reference for evaluating the wave effects.

As mentioned in Section 3.3, the **rotational speed** of propellers is set fixed with constant value (8.819 RPS) and the rudder is controlled by an **autopilot** shown in Eqn. (1). The initial flow state of the zigzag maneuver computation is from the stable state of self-propulsion condition, then the ship model is released in 6DoF with specified rudder control to achieve the zigzag maneuver motion.

Fig. 7 shows the time histories of ship yaw motion and **rudder angle** for the 10/10 zigzag maneuver in calm water simulation. The comparison of main parameters for standard zigzag maneuver in calm water is depicted in Table 4. Good agreement between the CFD results and experimental measurements by Experimental Fluid Dynamics (EFD) is achieved in terms of the time to execute rudder, the overshoot angle and the period to complete one zigzag turn. Despite the overall agreement, the overshoot angle is underestimated by 21.6% (1st OSA) and 18.1% (2nd OSA), while the time to check yaw as well as the period is overestimated by the simulation. The discrepancies can be explained by the different settings between the present simulations and the experiment. Unlike the experiments, the simulation adopts a **constant rotational speed** of propellers, which directly affects the approaching speed during the zigzag maneuver and further leads to the discrepancy of the time to check yaw and the period.



[Download : Download high-res image \(152KB\)](#)

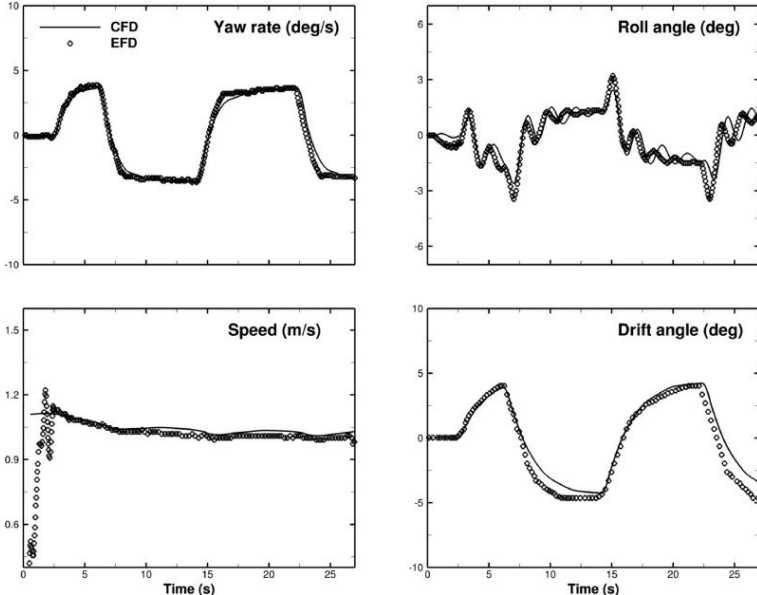
[Download : Download full-size image](#)

Fig. 7. Time history of rudder deflection and yaw angle in calm water from EFD (dashed lines) or CFD (solid lines) (A, B, C, D correspond to the time of first overshoot angle, the first time experience zero yaw, the time of second overshoot angle and the second time cross zero yaw, respectively).

Table 4. Comparison of main parameters for standard 10/10 zigzag maneuver in calm water.

Parameters	EFD	CFD
1 st OSA (deg)	2.31	1.81
2 nd OSA (deg)	2.10	1.72
T(1 st OSA) (s)	6.83	6.97
T(2 nd OSA) (s)	14.85	15.01
Period (s)	16.87	17.05

More differences between the CFD and EFD can be found in the time variations of ship motions and speeds, as shown in Fig. 8. The initial state of the experiment differs a lot from the simulations, especially for the ship speeds, which makes sense for the discrepancies in the two conditions. Apparently, there is some uncertainty on how accurately the nominal approach speed has been achieved in the experiments. Instead the time is measured from the start of the EFD maneuver and the CFD results are shifted a small amount to match the first rudder execution from port to starboard. After the large rudder deflection, the transient due to different initial conditions between CFD and EFD is weakened. For the time histories of yaw rate, it can be obviously seen that the predicted yaw rate is smaller at the turning points, which lead to the underestimation of overshoot angle shown in Fig. 7. The main difference for the roll and drift angle is the phase shift compared with the measurements, where the predicted results are delayed in time. The predicted peak value for roll angle is 2.43° compared with the measurement data of 3.20°.



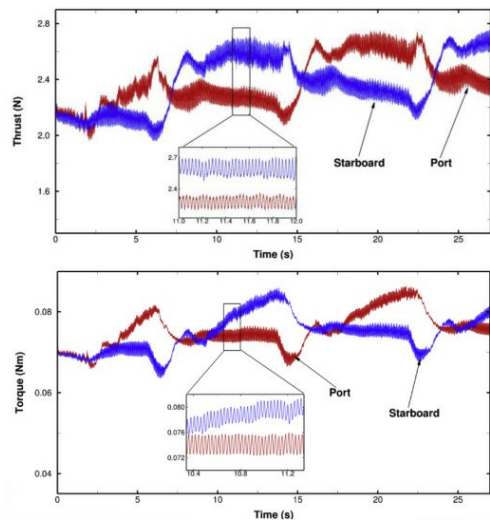
[Download : Download high-res image \(548KB\)](#)

[Download : Download full-size image](#)

Fig. 8. Predicted ship motions for zigzag maneuver in calm water.

Though little discrepancies exist, the present CFD results for the zigzag maneuver in calm water is promising compared with the available experimental data and can lay a good foundation for the numerical simulations of free-running zigzag maneuver in waves.

Fig. 9 illustrates the time histories of thrust and torque during the zigzag simulation in calm water. Both thrust and torque are evidently related to the ship motions and rudder execution. For instance, when the ship experiences rudder execution, the thrust and torque of the rotating propeller will show significant difference, which is mainly due to the large flow disturbance around the propeller caused by the rudder. The different behavior of port and starboard side propellers can be better understood through the local flow shown later. Besides, high frequency fluctuations in thrust and torque that correlate to the blade passage frequency are presented, which can be obviously seen in the viewport. The thrust and torque curves for both propellers can give a better illustration of the propulsion performance during the zigzag maneuver in calm water.

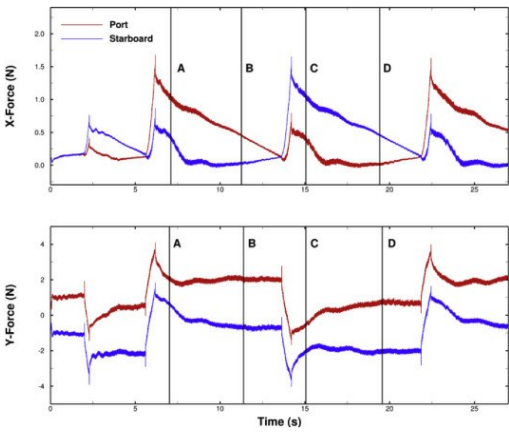


[Download : Download high-res image \(613KB\)](#)

[Download : Download full-size image](#)

Fig. 9. Propulsion performance in calm water condition.

The time histories of predicted rudder resistance and lateral rudder force are shown in Fig. 10. Every time the rudder is executed, there is a peak rudder resistance and lateral force. Another feature is that both the resistance and lateral force show alternate behaviors. At the beginning, the ship is advancing straight forward and the hydrodynamic forces are almost the same and symmetric. After the execution of rudders, the ship response to the corresponding rudder force and making highly difference of the wake flow around twin rudders. Due to the auto-pilot of zigzag maneuver, the rudder force changes alternatingly as shown in Fig. 10.

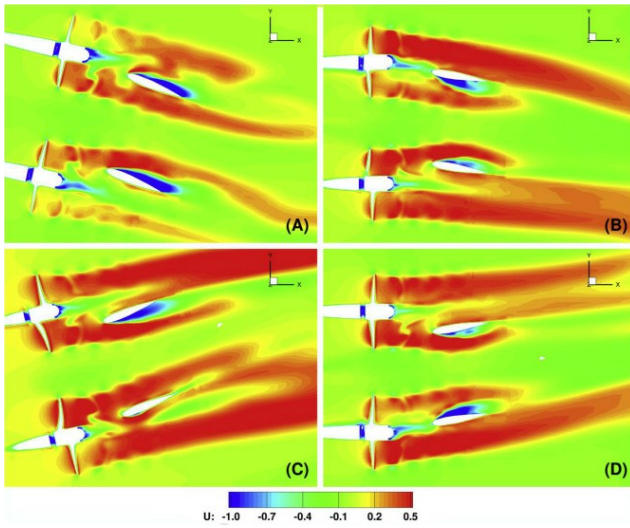


[Download : Download high-res image \(371KB\)](#)

[Download : Download full-size image](#)

Fig. 10. Time histories of rudder forces during zigzag maneuver in calm water (A, B, C, D correspond to the time of first overshoot angle, the first time experience zero yaw, the time of second overshoot angle and the second time cross zero yaw, respectively).

To help understand the hydrodynamic performance of twin propellers and rudders shown in Figs. 9 and 10, the wake region around twin propellers and rudders on a horizontal plane is shown in Fig. 11. Four typical time instants A, B, C, D as shown in Fig. 10 are adopted to analyze the results. It is obvious that the inflow for twin propellers show much difference at different time and oblique inflow occurs frequently, which lead to the highly difference for the thrust and torque variation. For the rudder forces, it is found that at instant A and B, the flow around the port side rudder, obviously, is much more complex than that on the starboard side. This well explains the larger resistance and lateral force from instant A to B for port side rudder. As for instant C and D, the flow field shows the opposite features, and the starboard side rudder experiences larger resistance and lateral force. The flow visualization can give a general description of the hydrodynamic behavior for twin propellers and rudders.



[Download : Download high-res image \(1MB\)](#)

[Download : Download full-size image](#)

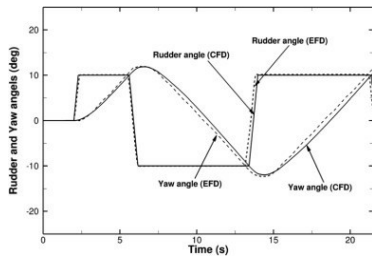
Fig. 11. Horizontal section of wake region around twin propellers and rudders during one zigzag period in calm water (A, B, C, D correspond to the time of first overshoot angle, the first time experience zero yaw, the time of second overshoot angle and the second time cross zero yaw, respectively).

4.3. Zigzag maneuver in waves

The simulation of free-running zigzag maneuver in waves mainly involves two parts: first is the same wave steepness with three different wave lengths, which follows the same conditions as in the experiments; the other one is the same wave height with three different wave lengths as shown in Table 2. The former case is simulated to investigate the effect of different wave length on the free-running ship maneuver and to validate the CFD results by comparing with the available experimental data. The latter one is conducted to study the influences of the wave height on the maneuvering performances. This section firstly presents the motion performances of the zigzag maneuver in different waves, where time histories of ship motions, speeds, yaw rate and rudder deflection are discussed in detail. Then the forces during the maneuvering simulation is used to investigate the hydrodynamic performances for free-running ship maneuver in waves, where the ship resistance, the propulsion performance (thrust and torque), and the forces on twin rudders in different waves are presented. Finally, detailed flow visualizations, e.g. wave elevation, wake profiles and vortical structures are given to further explain the hydrodynamic effects on ship maneuvering performance under different incident wave conditions.

4.3.1. Motions

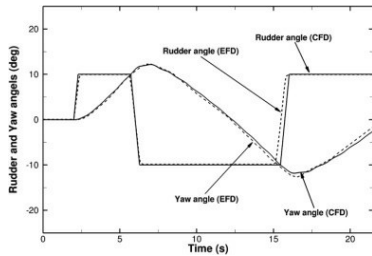
Fig. 12, Fig. 13, Fig. 14 show the time histories of yaw and rudder angle in different incident waves with the same wave steepness of 0.02. The CFD results show an overall agreement to the experiment measurements for all wave conditions, though some discrepancies are observed for both yaw and rudder angle. Same as in the calm water case, the predicted period to complete one zigzag turn is slightly overestimated for all the three wave conditions.



[Download : Download high-res image \(151KB\)](#)

[Download : Download full-size image](#)

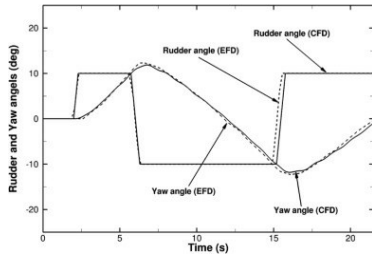
Fig. 12. Rudder execution and yaw angle in waves of $\lambda/L_{WL} = 0.5$.



[Download : Download high-res image \(145KB\)](#)

[Download : Download full-size image](#)

Fig. 13. Rudder execution and yaw angle in waves of $\lambda/L_{WL} = 1.0$.



[Download : Download high-res image \(143KB\)](#)

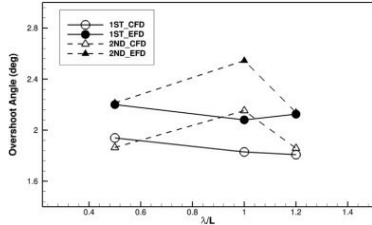
[Download : Download full-size image](#)

Fig. 14. Rudder execution and yaw angle in waves of $\lambda/L_{WL} = 1.2$.

Detailed quantities, such as overshoot angles (OSA) and period of a standard zigzag maneuver, are listed in [Table 5](#). Both first (1st) and second (2nd) overshoot angles are under-estimated from 11.9% to 15.8%, while the absolute error is small according to the value of yaw at time of overshoot angle (2.1%–3.1%). [Fig. 15](#) demonstrates the first and second overshoot angles of three different wave lengths, where the total trend matches very well with the measurements. The parameters of period to complete one zigzag turn can be accurately predicted with an error varies from 0.56% to 1.54%.

Table 5. Comparison of 1st and 2nd overshoot angles and period in waves.

λ/L_{WL}	1st OSA		YAW		2nd OSA		YAW		Period
	(deg.)	(1st OSA)	(deg.)	(2nd OSA)	(deg.)	(2nd OSA)	(deg.)	(2nd OSA)	
0.5	CFD	1.9391	11.9391	1.8641	11.8641	1.8641	11.8641	1.8641	15.7565
	EFD	2.2005	12.2005	2.2136	12.2136	2.2136	12.2136	2.2136	15.6685
1.0	CFD	1.8293	11.8293	2.1533	12.1533	2.1533	12.1533	2.1533	20.0388
	EFD	2.0810	12.0810	2.5454	12.5454	2.5454	12.5454	2.5454	19.7724
1.2	CFD	1.8081	11.8081	1.8582	11.8582	1.8582	11.8582	11.8582	19.4279
	EFD	2.1256	12.1256	2.1382	12.1382	2.1382	12.1382	12.1382	19.2901



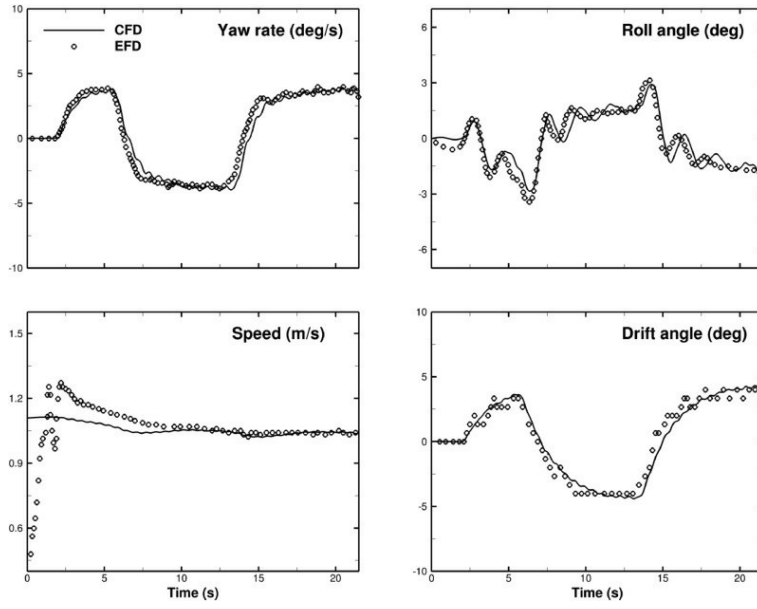
[Download : Download high-res image \(107KB\)](#)

[Download : Download full-size image](#)

Fig. 15. Comparisons of overshoot angles in different waves.

[Fig. 16](#), [Fig. 17](#), [Fig. 18](#) show the time histories of ship motions, yaw rate, instantaneous ship speed and drift angle under different wave conditions. The predicted results shown as solid lines are compared with the experimental data represented by circles. CFD predictions match well with the measurements except for the large discrepancies at the beginning, which have been discussed in the

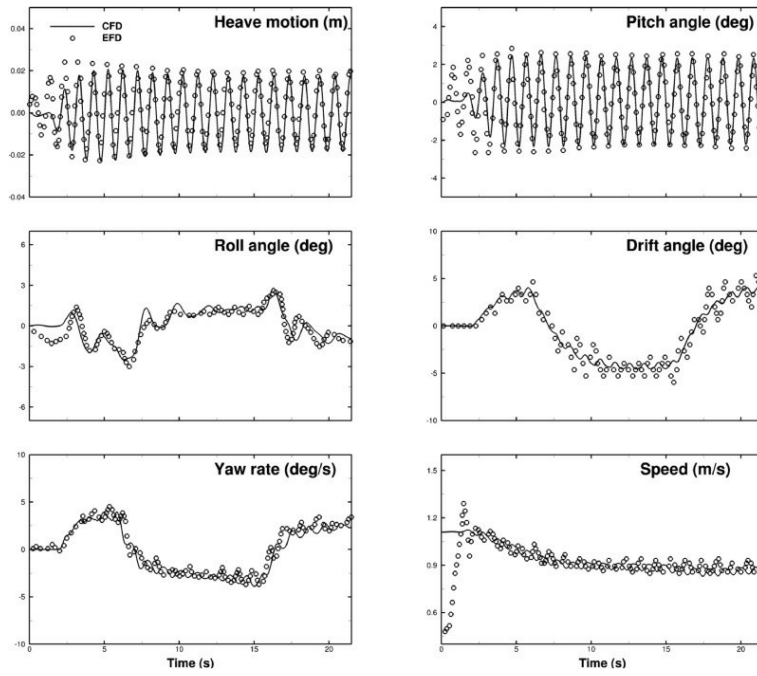
calm water case. The high frequency wave-induced motions and low frequency maneuvering motion can be observed in the time variation data, where the short wave indicates the smallest motion response. The wave induced oscillations in longer incident waves ($\lambda/L_{WL} = 1.0, \lambda/L_{WL} = 1.2$) are significant for the heave, pitch, drift, yaw rate and ship instantaneous speed. In order to characterize the wave effects on the free-running zigzag maneuvers, the Fourier Series (FS) (Shen and Wan, 2013; Tezdogan et al., 2015) are used to analyze the ship motions and velocities due to waves. The peak value of roll motions, 1st harmonic FS term of heave and pitch (taken as the mean fluctuation amplitude) and the mean value of ship speed represented by the 0th harmonic FS term are listed in Table 6. In addition, the comparison between time histories of ship motions and velocities in calm water and waves are shown in Fig. 19.



[Download : Download high-res image \(506KB\)](#)

[Download : Download full-size image](#)

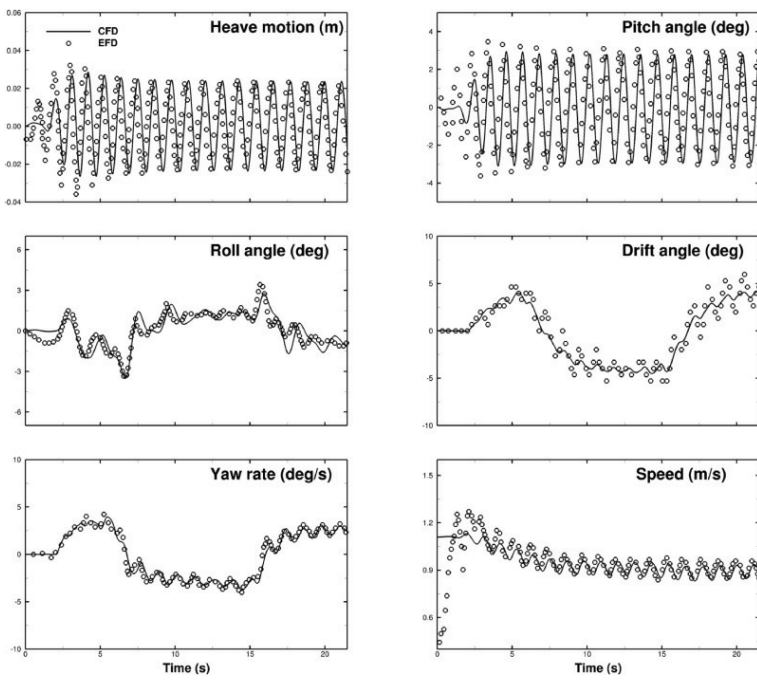
Fig. 16. Comparison of yaw rate, roll, ship speed and drift angle in waves of $\lambda/L_{WL} = 0.5$.



[Download : Download high-res image \(867KB\)](#)

[Download : Download full-size image](#)

Fig. 17. Comparison of heave, pitch, roll, drift motions, yaw rate and instantaneous ship speed in waves of $\lambda/L_{WL} = 1.0$.



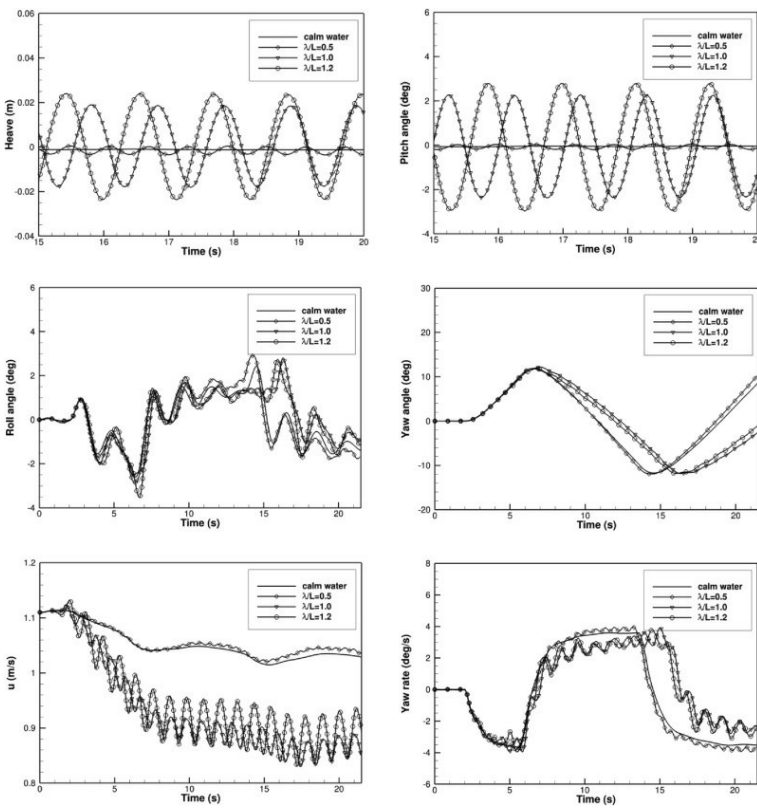
[Download : Download high-res image \(943KB\)](#)

[Download : Download full-size image](#)

Fig. 18. Comparison of heave, pitch, roll, drift motions, yaw rate and instantaneous ship speed in waves of $H/L_{WT} = 1.2$.

Table 6. Roll, heave, pitch and ship speed in different wave lengths.

λ/L_{WT}	Roll (deg)		Heave ($\cdot 10^{-3}$ m)		Pitch (deg)		Speed (m/s)	
	Min	Max	(1st FS)	(1st FS)	(1st FS)	(0th FS)		
0.5	-2.8491	2.9069	0.1799		0.1065		1.0350	
1.0	-2.6257	2.8037	1.8234		2.2911		0.8675	
1.2	-3.5198	2.7372	2.3883		2.8690		0.8919	



[Download : Download high-res image \(1MB\)](#)

[Download : Download full-size image](#)

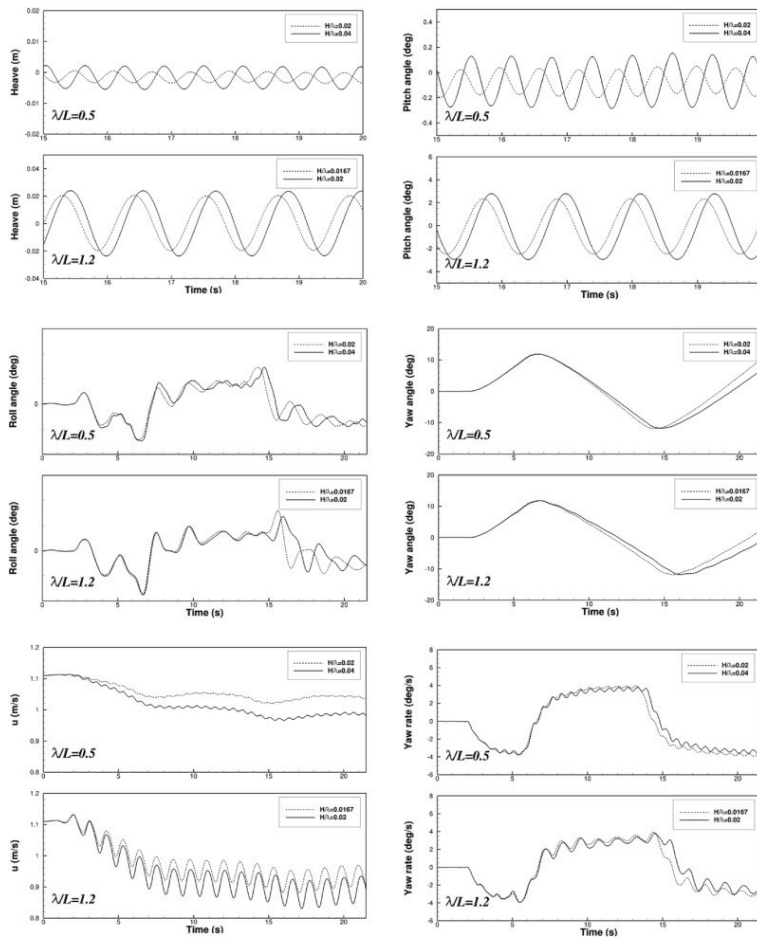
Fig. 19. Comparisons of ship motions under different wave lengths ($H/\lambda = 0.02$).

As shown in Fig. 17, Fig. 18 and Table 6, the heave and pitch motions quickly reach an apparently periodic wave-induced motions after the waves are fully generated in the computational domain. The heave and pitch motions under different wave conditions considered in Fig. 19 are localized to a smaller time scale with the consideration of better understanding the wave-length effects on the ship

performance. The mean amplitude of the oscillations of both heave and pitch motions represented by the 1st harmonic F_S shows strong relations with the wave lengths, where the amplitudes increase with the increasing of wave length. In addition, the heave and pitch motions can be enlarged significantly when the wave length is around one ship length. For example, the mean amplitude of heave in waves of $\lambda/L_{WL} = 1.0$ and $\lambda/L_{WL} = 1.2$ can be increased by 913.6% and 1227.6%, respectively. The phenomenon can be observed from both the predicted results and the measurements. The CFD predictions of roll angle match the total trend with the measurements with the peak values slightly underestimated. The drift angle, which is defined as the angle between the axis of a ship when turning and the tangent to the path on which it is turning, is usually used to characterize the turning quality. As shown in the figures, the fluctuations of measured drift angle due to the incident waves is larger than that of the CFD results. This indicates that the ship model is easier to turn in the experiments than the computations, which can explain the under-estimation of the overshoot angles shown in Table 5.

As for the yaw rate, the present simulation results are promising compared with the available data, where both the low frequency maneuvering rate and the high frequency wave-induced rate are accurately resolved. The speed loss is a main character for ship advancing in waves and it can be obtained by the ship instantaneous speed shown in Fig. 16, Fig. 17, Fig. 18. The mean value of the speed is using the 0th harmonic term of F_S which is listed in Table 6. The speed loss in waves of $\lambda/L_{WL} = 0.5, \lambda/L_{WL} = 1.0, \lambda/L_{WL} = 1.2$ are 6.76%, 21.85% and 19.65%, respectively. The comparisons of time histories of the ship instantaneous speed are shown in Fig. 19. The case with largest wave length undergoes the largest amplitude of fluctuations while the case with wave length identical to the ship length experiences the largest speed loss. The ship instantaneous speed is closely related to the period to complete one zigzag turn. Hence, there is an obvious phase shift for the results of roll, yaw, yaw rate. Corresponding to the speed loss, the wave conditions of $\lambda/L_{WL} = 1.0$ experiences the longest period 20.0388s compared with 15.7565s of $\lambda/L_{WL} = 0.5$ and 19.4279s of $\lambda/L_{WL} = 1.2$. Above all, CFD results of ship speeds follow the behavior of EFD fairly well, even though there is some uncertainty on how accurately the nominal approach speed has been achieved in the experiments.

Apart from the free-running zigzag maneuver in waves with the same wave steepness, the simulations are also conducted for different wave heights of the three wave lengths (described in Table 2). These conditions are used to investigate wave height effects on the free-running zigzag maneuver. Fig. 20 illustrates heave, pitch, roll, yaw, instantaneous ship speeds and yaw rate with different wave heights but the same wave length during the simulation time.



[Download : Download high-res image \(1MB\)](#)

[Download : Download full-size image](#)

Fig. 20. Comparisons of ship motions under different wave heights.

Table 7 summarizes the peak values of roll angle, overshoot angles, the mean value of the amplitude of heave and pitch as well as the mean value of the ship speeds. The amplitudes of heave and pitch motions obtained by the 1st harmonic F_S term show consistent growth with the wave height. For instance, in the short wave cases the wave steepness of 0.04 experiences almost twice than the wave steepness of 0.02. In general, the different wave heights for the same wave length means the wave contains different energy. Therefore, when encountering the steeper wave, it costs more power for ship to advance forward. Consequently, the mean value of ship speed obtained by the 0th harmonic F_S term of instantaneous ship speed is larger with the lower wave height. Meanwhile, the speed loss in short waves are 6.76% and 11.94 for the wave steepness of 0.02 and 0.04 respectively, and in waves of $\lambda/L_{WL} = 1.2$, the speed loss are 16.19% and 19.65% with wave steepness of 0.0167 and 0.02, respectively. Due to the different performance with the speeds, the discrepancies shown in the time histories of roll, yaw and yaw rate in Fig. 20 are mainly the time delay under higher wave condition, where the wave-induced amplitude of oscillations are also larger than that in lower wave case.

Table 7. Comparisons of main parameters in different waves.

λ/L_{WL}	H_s/λ	Roll (deg.)		OSA (deg.)		Heave (m)	Pitch (deg.)	Speed (m/s)
		Min	Max	1st	2nd			
0.5	0.02	-2.8491	2.9069	1.9391	1.8641	0.1799	0.1065	1.0350
	0.04	-2.9344	2.9226	1.8892	1.7905	0.3624	0.2006	0.9775
1.0	0.02	-2.6257	2.8037	1.8293	2.1533	1.8234	2.2911	0.8675
	0.04	-3.4675	3.1960	1.8281	1.8797	2.0075	2.4128	0.9303
1.2	0.02	-3.5198	2.7372	1.8081	1.8582	2.3883	2.8690	0.8919
	0.04	-3.5200	2.7374	1.8082	1.8583	2.3884	2.8691	0.8920

4.3.2. Forces

The hydrodynamic loads acting on the fully appended free-running ship can directly reflect the motion behavior during the zigzag maneuver in waves. At the beginning, the forces in the case of the wave length equals ship length are adopted to analyze the hydrodynamic performance.

Fig. 21 presents the **longitudinal forces** on **ship hull**, propeller and rudder, where the propeller force or rudder force are the **resultant force** on the twin propeller or the twin rudder, respectively. As can be seen from the figure, the ship resistance takes the main part of the total resistance, and the large fluctuations lead to the oscillations of ship speeds shown in **Fig. 17**.

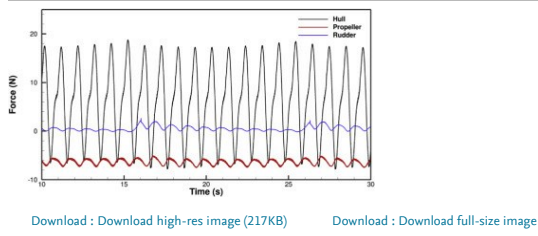


Fig. 21. Comparison of **longitudinal forces** on **ship hull**, **propeller** and **rudder**.

To further analyze the propulsion performance, the predicted propulsion forces are presented in **Fig. 22** during the simulation time. Both thrust and torque are evidently related to the ship motions (high frequency), rudder execution (low frequency) and wave frequency (medium frequency). Different from the calm water case, the thrust and torque curves show significant fluctuations with wave frequency and the mean value increase considerably. Wave-induced fluctuations can be as large as the fluctuation due to low-frequency maneuvering motion. High frequency fluctuations in thrust and torque that correlate to the blade passage frequency can also be captured, which can be seen in the partial enlarged view. The thrust and torque curves for both side propellers can give a better description of the propulsion performance during the zigzag maneuver in waves, where the local flow around twin propellers and rudders can change a lot due to the rudder deflection and ship maneuvering motion.

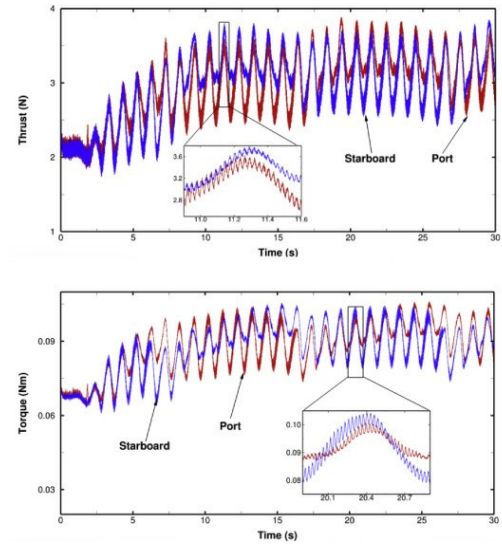


Fig. 22. Time histories of thrust (up) and torque (down) coefficients for zigzag maneuver in waves of $\lambda/L_{WL} = 1.0$.

Forces acting on twin rudders during zigzag maneuver in waves are depicted in **Fig. 23**. Compared with the calm water case, both rudder resistance and lateral force follow the behavior of the trend, while the fluctuations due to the incident waves are remarkable. The force amplitude induced by the waves can as large as the force due to rudder execution, which indicates that the wave effect is of great importance during the zigzag motion. CFD simulations of free-running ship maneuver in waves take most of the effects into account, such as **viscous flow**, resistance, rudder forces, propeller loads, wave effects etc. As a result, the present simulations can capture the unsteady behavior of the hydrodynamic loads. The detailed information of the forces acting on the twin-screw fully append ship presented above can give a better understanding of the hydrodynamic behavior for the free-running ship maneuver in waves. However, the lack of experiment data for forces and moments of ship hull, propellers and rudders prevent the validation, and so this phenomenon needs further investigations.

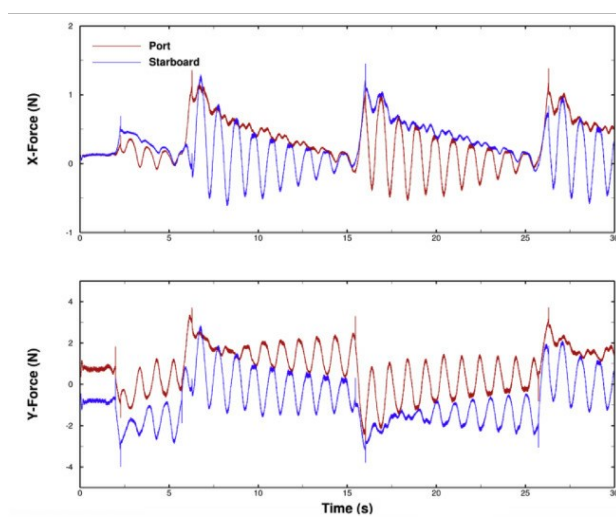
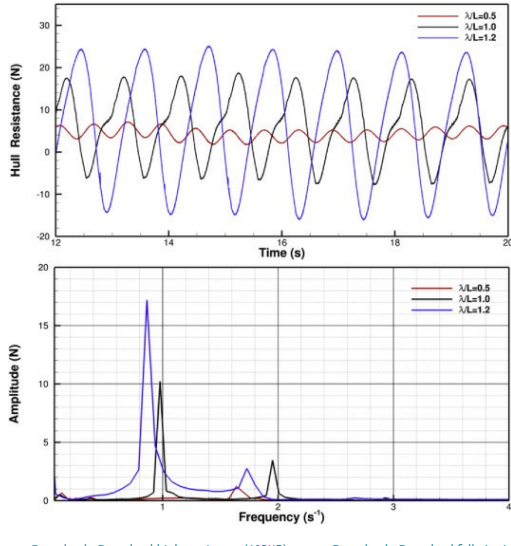


Fig. 23. Comparison of port and starboard rudder forces in waves of $\lambda/L_{WL} = 1.0$.

Apart from the wave condition of $\lambda/L_{WL} = 1.0$ discussed above, the hydrodynamic behavior with different wave lengths are also compared to analyze the wave-length effects on the free-running zigzag maneuver. **Fig. 24** shows the time histories of ship resistance with three different wave lengths but the same wave steepness 0.02. **Fast Fourier transform** (FFT) of the time histories of the ship resistance is used to identify the main dominant frequencies associated with the unsteady behavior. As can be seen from the results of FFT, the dominant frequency for all the conditions are the wave encounter

frequency. A secondary frequency is detected for the waves of $\lambda/L_{WL} = 1.0$ and $\lambda/L_{WL} = 1.2$, in which the crest is most evident for the case of $\lambda/L_{WL} = 1.0$. This phenomenon can also be observed in the time histories of the ship resistance, which is mainly due to the nonlinearity of the free-running ship in waves. As maybe occurred in most occasions, the **nonlinear effect** is caused by the ship motions, or so-called radiation effects, but in this case, the frequencies of ship motions are not correlated with the secondary frequency. The flow visualizations show that wave breaking occurs when ship bow experiences the wave crest and a second wave crest appears before the incident wave crest. This strong **nonlinear phenomenon** leads to the high frequency effect show in the time histories of ship resistance.

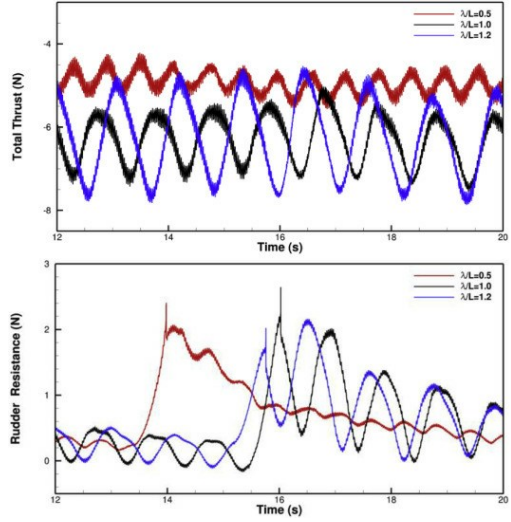


[Download : Download high-res image \(602KB\)](#)

[Download : Download full-size image](#)

Fig. 24. Comparison of ship resistance (up) and FFT (down) in different waves.

Fig. 25 presents the total thrust and rudder resistance in different waves by adding the port side and starboard side value. Similar to the ship resistance, the fluctuation amplitude of total thrust and rudder resistance is larger when the wave length increases. The rudder resistance experiences the transition when the rudder executes, which has been discussed in the calm water case. In order to quantitatively analyze the wave-length effects on the hydrodynamic loads on the free-running ship maneuver, the *FS* is used for the comparisons for the ship resistance, total thrust and rudder resistance (shown in Table 8). The mean value of the ship resistance and total thrust for waves of $\lambda/L_{WL} = 1.0$ is almost the same with waves of $\lambda/L_{WL} = 1.2$, while the mean amplitude of fluctuations obtained by the 1st harmonic FS term can be enlarged by 80.5% and 66.1% in the longer wave length case.



[Download : Download high-res image \(636KB\)](#)

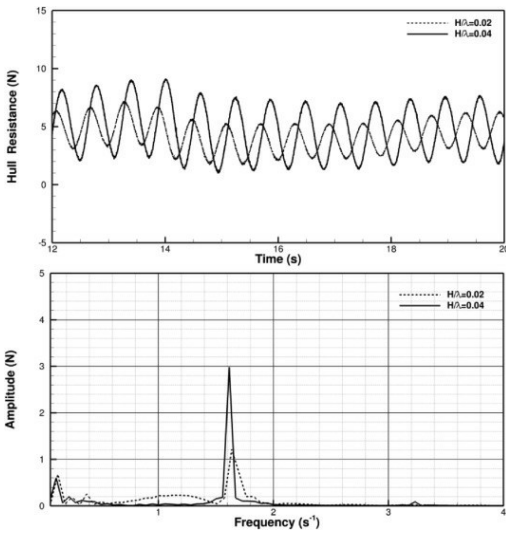
[Download : Download full-size image](#)

Fig. 25. Comparisons of total thrust (upper) and rudder resistance (lower) in different waves.

Table 8. Comparisons of hydrodynamic loads in different waves.

λ/L_{WL}	H/λ	Ship resistance (N)		Total thrust (N)		Rudder resistance
		0th FS	1st FS	0th FS	1st FS	0th FS (N)
0.5	0.02	4.225	1.577	-4.935	0.281	0.740
1.0	0.02	5.902	10.335	-6.346	0.763	0.545
1.2	0.02	5.924	18.657	-6.288	1.267	0.521

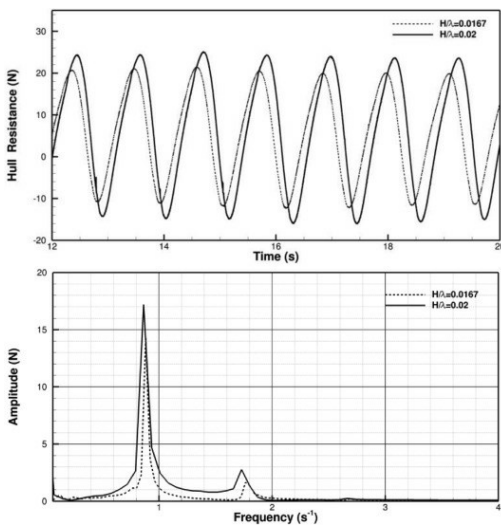
Apart from the hydrodynamic loads with different wave lengths, the time histories of ship resistance with different wave heights are shown in Fig. 26, Fig. 27. It is clear that the wave height can significantly enlarge the ship resistance, which will further lead to the larger speed loss discussed in Section 4.3.1.



[Download : Download high-res image \(499KB\)](#)

[Download : Download full-size image](#)

Fig. 26. Comparison of ship resistance (up) and FFT (down) in different wave heights with wave length of $\lambda/L_{WL} = 0.5$.



[Download : Download high-res image \(506KB\)](#)

[Download : Download full-size image](#)

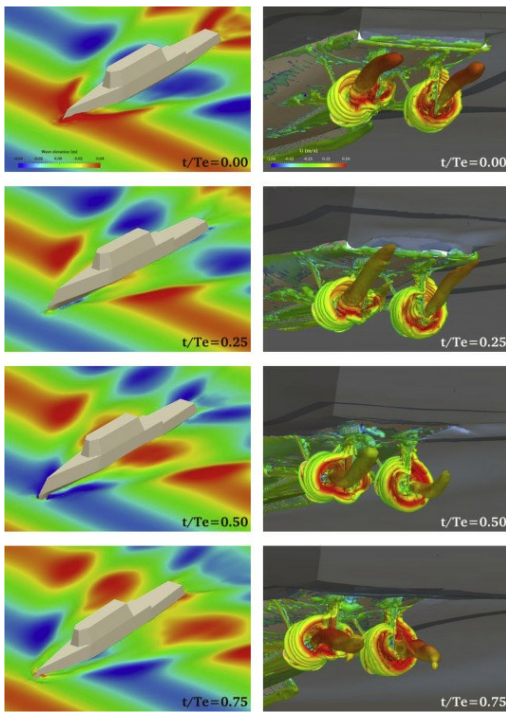
Fig. 27. Comparison of ship resistance (up) and FFT (down) in different wave heights with wave length of $\lambda/L_{WL} = 1.2$.

FFT analysis is also applied for the time histories of the ship resistance under different wave conditions to identify the main dominant frequencies associated with the unsteady behavior. As can be seen from the results of FFT (Fig. 26), the dominant frequency is slightly smaller in larger wave height condition. It can be concluded that the wave-height effects on the free-running ship maneuver are the hydrodynamic load amplitude and the dominant frequency.

4.3.3. Flow visualizations

As mentioned in the introduction, experiments still play an important role in the research of free-running ship maneuver, especially in waves. Nevertheless, CFD approaches are becoming more and more attractive with its improvements of the capabilities and the large amount of data which can provide detailed visualization of the flow field.

Fig. 28 illustrates the four snapshots of free surface and vortical structures depicted by iso-surfaces of $Q = 100$ (Q criterion is the second invariant of the velocity gradient tensor) around twin rotating propellers and moving rudders during one encounter wave period with wave length equals ship length. The time instants are chosen from 13.95s to 14.67s with respect to the simulation time and the rudder deflection stays constant value of -10° within the range. Views of the free surface and vortices can directly reflect the ship motion response in one wave period, where the ship model bows up after encountering with the wave crest and then the stern goes up when the ship advances from trough to crest. It is found that a new wave crest appears just before encountering the crest at $t/T_r = 0.75$ (T_r is the encountering period). This strong nonlinear phenomena leads to the obviously unsteady behavior shown in the FFT results of time histories of ship resistance mentioned in the last section. In addition, the propellers' tip, root and hub vortices interacted with the aligned rudders can be clearly observed. It can be noticed that the velocity of propeller vortices at $t/T_r = 0.25$ and $t/T_r = 0.50$ is lower than that at $t/T_r = 0$ and $t/T_r = 0.75$. The ship model in former situations is experiencing the wave trough, where the wave velocity is in the opposite direction of ship speed. Thus, the absolute velocity at propeller disk is reduced and further lead to the increase of the propeller load.



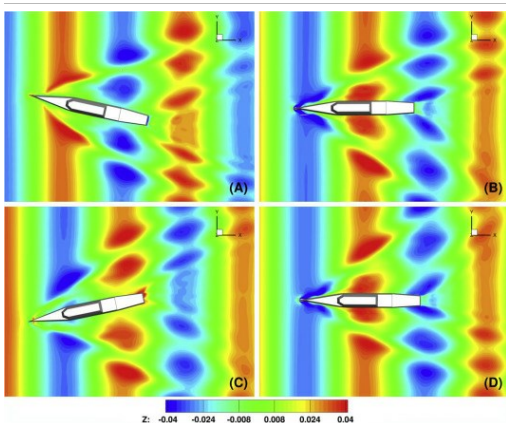
[Download : Download high-res image \(1MB\)](#)

[Download : Download full-size image](#)

Fig. 28. Snapshots of free surface (left column) colored by wave elevation and iso-surfaces of $Q = 100$ (right column) colored by axial velocity in one wave period.

On the contrary, the wave velocities are the same with the ship speed at $t/T_e = 0$ and $t/T_e = 0.75$, contributing to the reduce of the propeller loads. The changes of propeller loads discussed above can also be proven by the time histories of thrust and torque shown in Fig. 22. Moreover, the trajectory of hub vortices can reflect the trend of the ship motions.

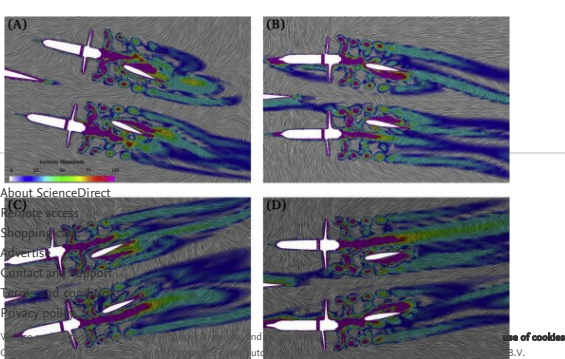
Fig. 29 shows the free surface colored with wave elevation for the standard 10/10 zigzag maneuver at four time instants corresponding to maximum and minimum yaw, zero yaw from starboard to port and port to starboard. It is clear that at time instant C, there is an obvious bow wave crest before encountering the incident wave crest. This phenomenon also lead to the nonlinear performance of the ship resistance shown in Fig. 24. In addition, Fig. 30 presents a closer look at wake flow around twin propellers and rudders colored by vorticity magnitude in the horizontal section at the rotational center during the four time instants mentioned in Fig. 29. Different from the calm water case, both side rudders experience much more complex flows and this can explain the large fluctuation during the most simulation time as shown in Fig. 23. The flow separation of twin rudders is evident and it is strongly affected by the hub vortices of the rotating propellers. At time instant A and C, the hub vortices of starboard side are disturbed by the aligned rudder and cause violent flows around the rudder. On the contrary, the port side hub vortices are significantly affected by the rudder at time instant B and D. Furthermore, the existence of the rudders can even affect the tip vortices, which can be clearly seen for the port side vortices at time instant A and B. The evident flow separations for the twin rudders and its encountering complex flows can play an important role for the ship maneuver in waves.



[Download : Download high-res image \(844KB\)](#)

[Download : Download full-size image](#)

Fig. 29. Wave elevation colored with wave elevation in waves of $\lambda/L_{WL} = 1.0$, (A) and (C) show maximum and minimum yaw, (B) and (D) are zero yaw, respectively.



[Download : Download high-res image \(1MB\)](#)

[Download : Download full-size image](#)

FEEDBACK

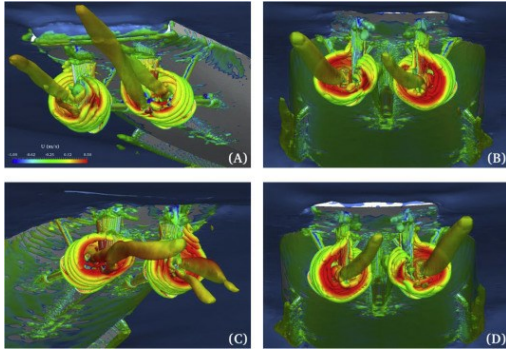


About ScienceDirect
Remote access
Shopping cart
Advertiser
Contact and support
Terms and conditions
Privacy policy
Helpdesk
ScienceDirect is a registered trademark of Elsevier B.V.

RELX™

Fig. 30. Horizontal section of wake region around twin propellers and rudders during one zigzag period in waves of $\lambda/L_{WL} = 1.0$.

The 3D vortical structures around ship hull, appendages, twin propellers and rudders in one zigzag period are shown in Fig. 31. The vortices are presented as iso-surfaces of $Q = 100$ colored by the axial velocity. The tip and hub vortices produced by the twin rotating propellers are evident during all the simulation time, and the strengths are stronger compared with the vortices separated from the bilge keels or skeg. Also of notice is the vortices at the root and tip of rudders. The rudder root vortices are partially caused by the artificial gap to gain enough interpolation cells, and when the rudder deflects, there is angle between the rudder and rudder root, which may cause the vortices. The rudder tip vortices are remarkable at time instant A and C, where the ship model meets the maximum and minimum yaw. Moreover, the rudder tip vortices are joined together with the hub vortices generated by the twin rotating propellers. This phenomenon is mainly caused by the ship motions, especially the pitch motion, where the vortices follow the ship trajectory while the near field vortices are redirected. Another feature of the vortical structures is the strong interaction between the propeller vortices and the aligned rudder. When the rudders turn to a different direction or the ship moving toward a different course, the disturbance may be the tip vortices or the hub vortices.

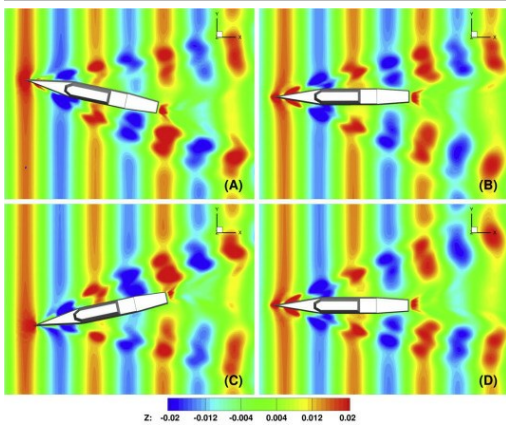


[Download : Download high-res image \(850KB\)](#)

[Download : Download full-size image](#)

Fig. 31. Iso-surfaces of $Q = 100$ colored with axial velocity for the zigzag maneuver in waves of $\lambda/L_{WL} = 1.0$.

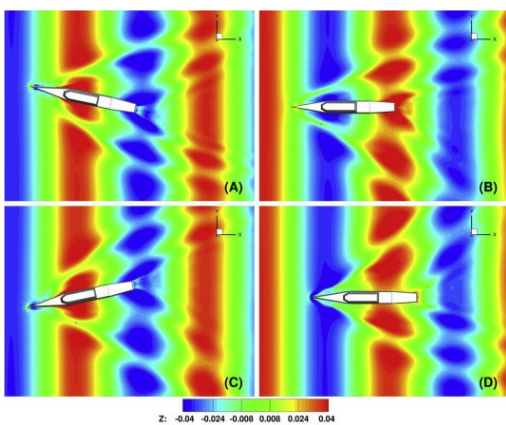
Besides, free surface elevations for the shorter wave and longer wave with the same wave steepness of 0.02 are shown in Fig. 32, Fig. 33. Compared with the previous case of wave length equals the ship length, the short wave case experience higher encountering frequency and the diffraction wave extends to a smaller region. It can also be observed that the wave patterns show strong relation with the maneuvering motion of the ship, especially at time instant B and D, where the ship hull is experiencing zero yaw angle. The highly difference of the wave distribution around ship hull also contributes to the lateral force and turning moment acting on the maneuvering ship. It can also be noticed that the ship bow meets the wave crest for all the four instants.



[Download : Download high-res image \(875KB\)](#)

[Download : Download full-size image](#)

Fig. 32. Wave elevation colored with wave elevation in waves of $\lambda/L_{WL} = 0.5$, (A) and (C) show maximum and minimum yaw, (B) and (D) are zero yaw, respectively.



[Download : Download high-res image \(848KB\)](#)

[Download : Download full-size image](#)

Fig. 33. Wave elevation colored with wave elevation in waves of $\lambda/L_{WL} = 1.5$, (A) and (C) show maximum and minimum yaw, (B) and (D) are zero yaw, respectively.

Fig. 33 shows the free surface elevations around free running ship in longer incident waves of $\lambda/L_{WL} = 1.5$. The mid-ship meets the wave crest for the time instant of A and C, where the ship is experiencing the maximum and minimum yaw angle. A similar phenomenon appears at time instant B, where a new wave crest forms before the ship bow experiences the wave crest. Compared with Fig. 32, the diffraction wave extends to a larger range and the ship wave-making, especially for the stern wave is relatively small compared to the incident waves. This can also explains the large wave induced oscillations of ship motions and velocities discussed in Section 4.3.1.

5. Conclusions and future work

This paper presents the direct simulations of free-running zigzag maneuver in both calm water and waves by using the CFD solver naoe-FOAM-SJTU coupled with dynamic overset grid technique. Open source toolbox waves2foam is utilized to generate the desired wave environment with the moving computational domain. Twin-screw fully appended ONR Tumblehome ship model is used for all the numerical simulations. With the capability of dynamic overset grids, the full 6DoF motion solver with maneuvering control is successfully applied to simulate the standard 10/10 zigzag maneuver with actual rotating propellers and rudders in various wave environments.

Grid convergence study for open water calculations and maneuvering in calm water is firstly performed to validate the CFD approach with the consideration of its simplicity compared with the wave conditions. Next, three wave lengths, i.e. $\lambda/L_{W,L} = 0.5$, $\lambda/L_{W,L} = 1.0$, $\lambda/L_{W,L} = 1.2$, are used in the simulations to investigate the wave-length effects on the free-running zigzag maneuver. The predicted ship motions for all the cases show remarkable good agreement with the free-running tests, which further indicates the reliability and feasibility of the present CFD approach with dynamic overset grid. The main wave-length effect is the speed loss and period to complete one zigzag turn, where the wave of $\lambda/L_{W,L} = 1.0$ meets the largest speed loss of 21.85% and longest period of 20.0388s. Wave induced motions are enlarged significantly when increasing the wave length, where the wave of $\lambda/L_{W,L} = 1.2$ experiences the largest wave induced oscillations of ship motions including speeds and yaw rate. In addition, different wave heights are also taken into account to study how the wave height affect the performance of free-running ship maneuver. With the same wave length, larger wave height causes larger hydrodynamic loads, larger motion response as well as larger speed loss. The wave-induced motion is almost proportional to the wave height. Since the CFD simulations can take most of the effects into account, strong unsteady and nonlinear behavior is found in the hydrodynamic loads acting on the hull, twin propellers and rudders. Propulsion forces and the rudder forces are also presented to illustrate the hydrodynamic performance during free-running zigzag maneuver in waves. Flow visualizations, such as wave elevations, wake flow around twin propellers and rudder, and vortical structures are presented to give a better description of the flow variation during the free-running zigzag maneuver in waves.

The main conclusion of the present work is that the present CFD solver naoe-FOAM-SJTU can be effectively used to handle problems with free-running zigzag maneuver in various wave conditions. Future work includes simulations of turning circle maneuver in waves in order to study the wave effects on the trajectory and the course, which are other important characteristic parameters for evaluating ship maneuverability in waves.

Acknowledgments

This work is supported by the National Natural Science Foundation of China ([51490675](#), [11432009](#), [51579145](#)), Chang Jiang Scholars Program ([T2014099](#)), Shanghai Excellent Academic Leaders Program ([17XD1402300](#)), Program for Professor of Special Appointment (Eastern Scholar) at Shanghai Institutions of Higher Learning ([2013022](#)), Innovative Special Project of Numerical Tank of Ministry of Industry and Information Technology of China ([2016-23/09](#)) and Lloyd's Register Foundation for doctoral student, to which the authors are most grateful.

[Special issue articles](#) [Recommended articles](#) [Citing articles \(30\)](#)

References

- ABS, 2006** ABS
American Bureau of Shipping: Guide for Vessel Maneuverability
(2006)
(Houston, USA)
[Google Scholar](#)
- Araki et al., 2012** M. Araki, H. Sadat-Hosseini, Y. Sanada, K. Tanimoto, N. Umeda, F. Stern
Estimating maneuvering coefficients using system identification methods with experimental, system-based, and CFD free-running trial data
Ocean. Eng., 51 (2012), pp. 63-84
<https://doi.org/10.1016/j.oceaneng.2012.05.001>
[Article](#) [Download PDF](#) [View Record in Scopus](#) [Google Scholar](#)
- Berberović et al., 2009** E. Berberović, N. van Hinsberg, S. Jakirlić, I. Roisman, C. Tropea
Drop impact onto a liquid layer of finite thickness: Dynamics of the cavity evolution
Phys. Rev. E, 79 (36306) (2009)
<https://doi.org/10.1103/PhysRevE.79.036306>
[Google Scholar](#)
- Broglia et al., 2015** R. Broglia, G. Dubbioso, D. Durante, A. Di Mascio
Turning ability analysis of a fully appended twin-screw vessel by CFD. Part I: single rudder configuration
Ocean. Eng., 105 (2015), pp. 275-286
<https://doi.org/10.1016/j.oceaneng.2015.06.031>
[Article](#) [Download PDF](#) [View Record in Scopus](#) [Google Scholar](#)
- Carrica et al., 2010** P.M. Carrica, A.M. Castro, F. Stern
Self-propulsion computations using a speed controller and a discretized propeller with dynamic overset grids
J. Mar. Sci. Technol., 15 (2010), pp. 316-330
[CrossRef](#) [View Record in Scopus](#) [Google Scholar](#)
- Carrica et al., 2012** P.M. Carrica, F. Ismail, M. Hyman, S. Bhushan, F. Stern
Turn and zigzag maneuvers of a surface combatant using a URANS approach with dynamic overset grids
J. Mar. Sci. Technol., 18 (2012), pp. 166-181
<https://doi.org/10.1007/s00773-012-0196-8>
[Google Scholar](#)
- Carrica et al., 2016** P.M. Carrica, A. Mofidi, K. Eloot, G. Delefortrie
Direct simulation and experimental study of zigzag maneuver of KCS in shallow water
Ocean. Eng., 112 (2016), pp. 117-133
<https://doi.org/10.1016/j.oceaneng.2015.12.008>
[Article](#) [Download PDF](#) [View Record in Scopus](#) [Google Scholar](#)
- Castro et al., 2011** A.M. Castro, P.M. Carrica, F. Stern
Full scale self-propulsion computations using discretized propeller for the KRISO container ship KCS
Comput. Fluids, 51 (2011), pp. 35-47
[Article](#) [Download PDF](#) [View Record in Scopus](#) [Google Scholar](#)
- Dubbioso et al., 2016** G. Dubbioso, D. Durante, A. Di Mascio, R. Broglia
Turning ability analysis of a fully appended twin-screw vessel by CFD. Part II: single vs. twin rudder configuration
Ocean. Eng., 117 (2016), pp. 259-271
<https://doi.org/10.1016/j.oceaneng.2016.03.001>
[Article](#) [Download PDF](#) [View Record in Scopus](#) [Google Scholar](#)
- Dubbioso et al., 2017** G. Dubbioso, R. Muscari, F. Ortolani, A. Di Mascio
Analysis of propeller bearing loads by CFD. Part I: straight ahead and steady turning maneuvers
Ocean. Eng., 130 (2017), pp. 241-259
<https://doi.org/10.1016/j.oceaneng.2016.12.004>
[Article](#) [Download PDF](#) [View Record in Scopus](#) [Google Scholar](#)
- Fonseca and Guedes Soares, 1998** N. Fonseca, C. Guedes Soares
Time-domain analysis of large-amplitude vertical ship motions and wave loads
J. Ship Res., 42 (1998), pp. 139-152
[CrossRef](#) [View Record in Scopus](#) [Google Scholar](#)
- Issa, 1986** R.I. Issa
Solution of the implicitly discretised fluid flow equations by operator-splitting
J. Comput. Phys., 62 (1986), pp. 40-65

ITTC, 2017a ITTC

Proposed tasks and structure of the 29th ITTC technical committees and groups

Proceedings of 28th International Towing Tank Conference. Wuxi, China (2017), pp. 393-408

[View Record in Scopus](#) [Google Scholar](#)

ITTC, 2017b ITTC

Uncertainty Analysis in CFD Verification and Validation Methodology and Procedures (No. 7.5-03-01-01)

(2017)

[Google Scholar](#)

Jacobsen et al., 2012 N.G. Jacobsen, D.R. Fuhrman, J. Fredsøe

A wave generation toolbox for the open-source CFD library: OpenFOAM®

Int. J. Numer. Methods Fluids, 70 (2012), pp. 1073-1088

[CrossRef](#) [View Record in Scopus](#) [Google Scholar](#)

Menter et al., 2003 F.R. Menter, M. Kuntz, R. Langtry

Ten years of industrial experience with the SST turbulence model

Turbul. Heat. Mass Transf., 4 (2003), pp. 625-632

[View Record in Scopus](#) [Google Scholar](#)

Mofidi and Carrica, 2014 A. Mofidi, P.M. Carrica

Simulations of zigzag maneuvers for a container ship with direct moving rudder and propeller

Comput. Fluids, 96 (2014), pp. 191-203

<https://doi.org/10.1016/j.compfluid.2014.03.017>[Article](#) [Download PDF](#) [View Record in Scopus](#) [Google Scholar](#)

Muscari et al., 2017 R. Muscari, G. Dubbioso, F. Ortolani, A. Di Mascio

Analysis of propeller bearing loads by CFD. Part II: transient maneuvers

Ocean. Eng., 146 (2017), pp. 217-233

<https://doi.org/10.1016/j.oceaneng.2017.09.050>[Article](#) [Download PDF](#) [View Record in Scopus](#) [Google Scholar](#)

Noack et al., 2009 R.W. Noack, D.A. Boeger, R.F. Kunz, P.M. Carrica

Sugar++: an improved general overset grid assembly capability

Proceedings of the 19th AIAA Computational Fluid Dynamics Conference. San Antonio TX (2009), pp. 22-25

[Google Scholar](#)

Pérez Arribas, 2007 F. Pérez Arribas

Some methods to obtain the added resistance of a ship advancing in waves

Ocean. Eng., 34 (2007), pp. 946-955

<https://doi.org/10.1016/j.oceaneng.2006.06.002>[Article](#) [Download PDF](#) [View Record in Scopus](#) [Google Scholar](#)

Sakamoto et al., 2012 N. Sakamoto, P.M. Carrica, F. Stern

URANS simulations of static and dynamic maneuvering for surface combatant: part 2. Analysis and validation for local flow characteristics

J. Mar. Sci. Technol., 17 (2012), pp. 446-468

<https://doi.org/10.1007/s00773-012-0184-z>[CrossRef](#) [Google Scholar](#)

Sanada et al., 2013 Y. Sanada, K. Tanimoto, K. Takagi, L. Gui, Y. Toda, F. Stern

Trajectories for ONR Tumblehome maneuvering in calm water and waves

Ocean. Eng., 72 (2013), pp. 45-65

<https://doi.org/10.1016/j.oceaneng.2013.06.001>[Article](#) [Download PDF](#) [View Record in Scopus](#) [Google Scholar](#)

Seo and Kim, 2011 M.-G. Seo, Y. Kim

Numerical analysis on ship maneuvering coupled with ship motion in waves

Ocean. Eng., 38 (2011), pp. 1934-1945

<https://doi.org/10.1016/j.oceaneng.2011.09.023>[Article](#) [Download PDF](#) [View Record in Scopus](#) [Google Scholar](#)

Shen and Wan, 2016 Z. Shen, D. Wan

An irregular wave generating approach based on naoe-FOAM-SJTU solver

China Ocean. Eng., 30 (2016), pp. 177-192

[CrossRef](#) [View Record in Scopus](#) [Google Scholar](#)

Shen and Wan, 2013 Z. Shen, D. Wan

RANS computations of added resistance and motions of a ship in head waves

Int. J. Offshore Polar Eng., 23 (2013), pp. 264-271

[View Record in Scopus](#) [Google Scholar](#)

Shen et al., 2015 Z. Shen, D. Wan, P.M. Carrica

Dynamic overset grids in OpenFOAM with application to KCS self-propulsion and maneuvering

Ocean. Eng., 108 (2015), pp. 287-306

<https://doi.org/10.1016/j.oceaneng.2015.07.035>[Article](#) [Download PDF](#) [View Record in Scopus](#) [Google Scholar](#)

Shen et al., 2014 Z. Shen, D. Wan, P.M. Carrica

RANS simulations of free maneuvers with moving rudders and propellers using overset grids in OpenFOAM

Proceedings of SIMMAN Workshop on Verification and Validation of Ship Maneuvering Simulation Methods. Lyngby, Denmark (2014)

[Google Scholar](#)

Simonsen et al., 2012 C.D. Simonsen, J.F. Otzen, C. Klimt, N.L. Larsen, F. Stern

Maneuvering predictions in the early design phase using CFD generated PMM data

Proceedings of the 29th Symposium on Naval Hydrodynamics (2012), pp. 26-31

[View Record in Scopus](#) [Google Scholar](#)

Sprenger et al., 2017 F. Sprenger, A. Maron, G. Delefertrie, T. van Zwijnsvoorde, A. Cura-Hochbaum, A. Lengwinat, A. Papanikolaou

Experimental studies on seakeeping and maneuverability of ships in adverse weather conditions

J. Ship Res., 61 (2017), pp. 131-152

[View Record in Scopus](#) [Google Scholar](#)

Tezdogan et al., 2015 T. Tezdogan, Y.K. Demirel, P. Kellett, M. Khorasanchi, A. Incecik, O. Turan

Full-scale unsteady RANS CFD simulations of ship behaviour and performance in head seas due to slow steaming

Ocean. Eng., 97 (2015), pp. 186-206

<https://doi.org/10.1016/j.oceaneng.2015.01.011>[Article](#) [Download PDF](#) [View Record in Scopus](#) [Google Scholar](#)

Investigations of self-propulsion in waves of fully appended ONR Tumblehome model

Appl. Math. Mech., 37 (2016), pp. 1345-1358

<https://doi.org/10.21656/1000-0887.370525>

[View Record in Scopus](#) [Google Scholar](#)

Free maneuvering simulation of ONR Tumblehome using overset grid method in naoe-fnam-SJTU solver

Proceedings of the 31th Symposium on Naval Hydrodynamics. Monterey, USA (2016)

[Google Scholar](#)

CFD simulations of free running ship under course keeping control

Ocean. Eng., 141 (2017), pp. 450-464

<https://doi.org/10.1016/j.oceaneng.2017.06.052>

[Article](#) [Download PDF](#) [View Record in Scopus](#) [Google Scholar](#)

Numerical computations of resistance of high speed catamaran in calm water

J. Hydronaut. Ser. B, 26 (2015), pp. 930-938

[https://doi.org/10.1016/S1001-6058\(14\)60102-5](https://doi.org/10.1016/S1001-6058(14)60102-5)

[Article](#) [Download PDF](#) [View Record in Scopus](#) [Google Scholar](#)

A numerical study on prediction of ship maneuvering in waves

Proceedings of 30th International Workshop on Water Waves and Floating Bodies. Bristol, UK (2015)

[Google Scholar](#)

[View Abstract](#)